Supplementary Materials

Stable Iridium Dinuclear Heterogeneous Catalysts Supported on Metal Oxide Substrate for Solar Water Oxidation

Yanyan Zhao[1†], Ke. R. Yang[2†], Zechao Wang[3,4#], Xingxu Yan[5,6#], Sufeng Cao[7#], Yifan Ye[8#], Qi Dong[1], Xizi Zhang[1], James E. Thorne[1], Lei Jin[3], Kelly L. Materna[2], Antonios Trimpalis[7], Hongye Bai[1], Sirine C. Fakra[8], Xiaoyan Zhong[4], Peng Wang[5], Xiaoqing Pan[6,6a], Jinghua Guo[8], Maria Flytzani-Stephanopoulos[7], Gary W. Brudvig[2*], Victor S. Batista[2*], Dunwei Wang[1*]

Correspondence to: dwang@bc.edu, gary.brudvig@yale.edu, victor.batista@yale.edu

More Experimental Methods

Preparation of Ir homogenous dimer complex (Ir homo-dimer)

Synthesis of Ir homo-dimer was based on previously established methods (1). The precursor, Cp*Ir[pyalc(OH)] (Cp*: pentamethylcyclopentadienyl, $C_5Me_5^-$, pyalc:2-(2'-pyridyl)-2-propanoate), was synthesized by a well-established procedure (1). A typical procedure for the formation of Ir homo-dimer is as follows: 0.024 g (0.049 mmol) of Cp*Ir[pyalc(OH)] was added to a 100 mL flask, and dissolved in 50.0 mL of water to form a 1 mM solution of Cp*Ir[pyalc(OH)]. The solution was stirred for approximately one minute at room temperature in air, forming a clear, red solution. Then, 1.07 g (5.00 mmol) of $NaIO_4$ was added to the solution (100 mM concentration with respect to $NaIO_4$), which immediately began bubbling. The solution was stirred at room temperature in air for two hours upon which the color of the solution changed from red to green to blue. UV-Vis absorption spectroscopy of the solution after two hours showed the expected absorption features for Ir homo-dimer, having a broad absorption around 600 nm (1).

Preparation of α-Fe_2O_3 substrate

A fluorine-doped tin oxide (FTO) substrate was soaked in a solution containing 0.15 M $FeCl_3$ (97%, Alfa Aesar) and 1 M $NaNO_3$ (99%, Alfa Aesar) with the backside covered by Kapton tapes. The reaction was carried out at 100 °C for 1 h. After thorough rinsing by deionized (DI) water, the substrate was annealed at 800 °C for 5 min to obtain α-Fe_2O_3. The process has been repeated another two times to obtain re-grown α-Fe_2O_3 for optimum performance (2).

HAADF-STEM image simulation

Multislice HAADF-STEM image simulations were performed using Dr. Probe software (3) on the basis of atomic models relaxed by first-principle DFT calculations as shown in Fig. 3 and using experimental imaging parameters. The Fe_2O_3 structural model for simulation consists of 6 Fe layers, corresponding to ca. 2 nm in thickness. The sample misalignment angle and the aberrations of the microscope were set to zero for the simulations. Structural models were visualized using the VESTA software (4).

X-ray Absorption Spectroscopy (XAS)

Ir L3-edge XAS data were recorded at the microprobe beamline 10.3.2 of the Advanced Light Source, Lawrence Berkeley National Laboratory (ALS, LBL). The storage ring was operated in top-off mode (1.9 GeV, 296 buckets, 500 mA). Using a Si (111) monochromator, the data collection was carried out in fluorescence mode for all samples under ambient conditions. An Ir foil (1st derivative taken at 11215.5 eV) and IrO_2 standard were measured for energy calibration purposes. The beam spot size was 15×3 μm^2 for XANES and EXAFS measurements.

The raw XAS data were deadtime corrected and calibrated using a suite of LabVIEW custom software available at the beamline. Data were subsequently analyzed using Athena Demeter version 0.9.24. The experimental data were fitted by EXAFS scattering path simulations using Artemis Demeter version 0.9.24 (5). The coordination number of Ir-O for IrO_2 standard was fixed at 6 to determine the amplitude reduction factor (S_0^2).

The work-up of XAS data to k-space and Fourier transformed R-space was done using a consistent methodology of background subtraction, post-edge normalization, conversion to k-space, and FT conversion in R-space. All sample data were refined using k^3-weighting, a Kaiser-bessel window k-range of 3-14 $Å^{-1}$ and R-range of 1.0-2.2 Å for the first shell fitting, R-range of 1.0-4.0 Å for the second shell fitting.

The S_0^2 value was determined to be 0.90 (fixed in all proceeding fits) by fitting the first Ir-O shell of the IrO_2 reference and fixing the CN parameter at 6. The Nyquist criterion was used to calculate the number of independent data points for each EXAFS spectrum that was fit. The number of dependent parameters was maintained to be less than or 1/2 the value of the maximum number of independent data points. Uncertainties in EXAFS fitting parameters were weighted by the square root of the reduced chi-squared value obtained for the simulated fit.

Computational details

Previous study has shown that the dominant termination of α-Fe_2O_3 in aqueous solution is the hydroxyl termination. Slab models were chosen to have 4 unit cells and full geometry relaxation was performed for the hydroxyl terminated α-Fe_2O_3 slab. A vacuum layer of about 20 Å was used to avoid the interactions between periodic images. A 3×3×1 Monckhorst-Pack type k-point grid was chosen for slab calculations. The fully optimized hydroxylated surface was used to study the absorption of Ir homo-dimer and Ir DHC, as well as the catalytic cycle of the reaction. During the optimization of the slab model, bottom several layers are fixed at the bulk position while the absorbed species and the top two Fe layers and two O layers are allowed to relax. Because of the strong d-electron correlation effects for Fe, the calculations were carried out with the DFT+U method, using the formalism suggested by Dudarev *et al.*(6). The parameter was set at U_{eff} = 4 eV to reproduce the experimental band gap of α-Fe_2O_3 (Table S2). For Ir, the U_{eff} parameter was set to 3 eV to reproduce the atomic magnetic moment of Ir homo-dimer while retaining the conductor property of IrO_2 (Fig. S17).

A supercell of 15 Å×15 Å×15 Å and 1×1×1 Monckhorst-Pack type k-point grid were used for the calculation of small molecules. The Gaussian smear method was used for molecule calculations and the σ value was chosen to be 0.1 eV. For Ir homo-dimer, a larger supercell of 30 Å × 30 Å × 30 Å was used to avoid artificial interactions between periodic images. For reaction steps involving H^+ and e^-, the computational hydrogen electrode (CHE) technique developed by Nørskov *et al.* was used to take into account the dependence of relative energies on pH and applied bias potential (7). The potential for oxidation of $H_2O(l) \rightarrow O_2(g) + 4H^+(aq) + 4e^-$ is calculated to 1.11 V, while the experimental value is 1.23 V. All potentials are given vs. RHE. We used this potential as an internal reference to obtain more reliable potentials for each oxidation process. The zero-point energy (ZPE) and entropic contributions are considered in the calculations of the reaction free energy. Partial frequency analysis was performed for the absorbed molecules (*OH_2, *OH, *O, *OOH, *OO) to obtained the zero-point energy correction. The entropies of $H_2O(l)$, $O_2(g)$, and $H_2(g)$ were used to consider the entropic contribution (8). The entropic contributions from absorbed species on the surfaces are small, so we omitted them, which is a common practice in the literature (9).

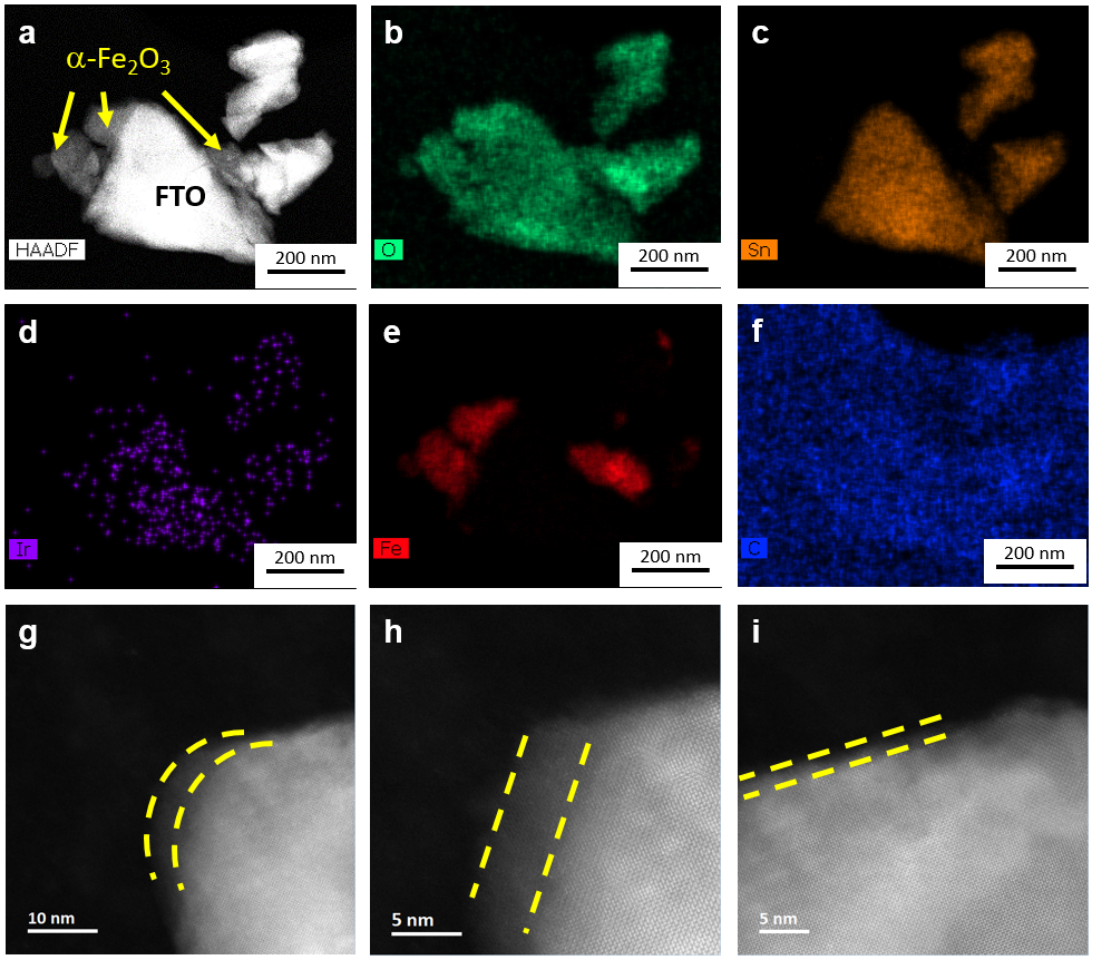

Fig. S1. STEM characterization of Ir intermediate on α-Fe_2O_3. (**a**) HAADF-STEM image and (**b-f**) EDS elemental mapping of O, Sn, Ir, Fe and C in the same region. The location of FTO and α-Fe_2O_3 are indicated in (**a**) with arrows. (**g-i**) HAADF-STEM images of Ir intermediate on α-Fe_2O_3. The yellow dashed lines in each images show the surface amorphous layer, which is formed as a result of the burning of organic ligands under electron beam irradiation. The Ir atoms are not observed on the surface due to the presence of this amorphous layer.

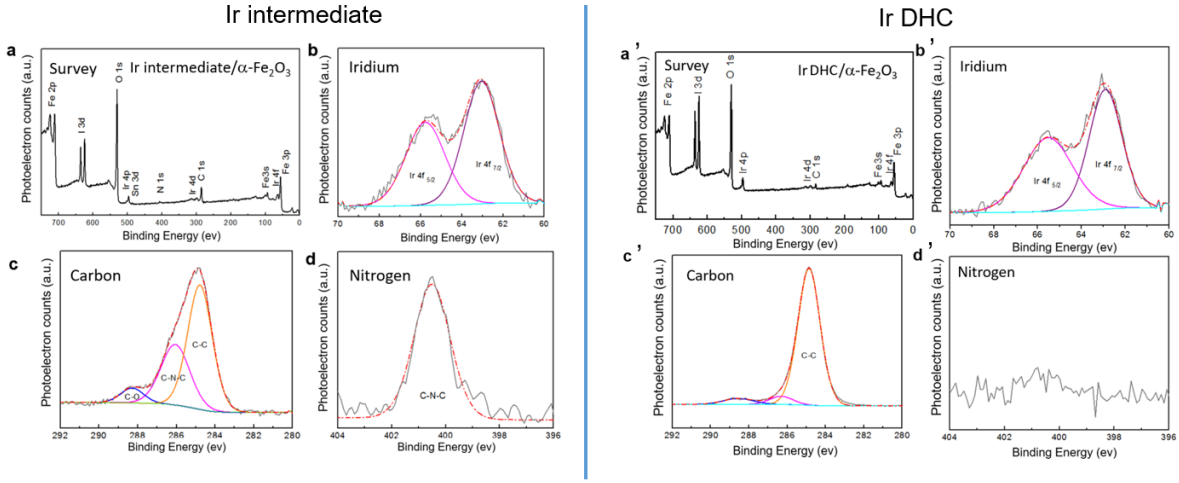

Fig. S2. XPS spectra of Ir intermediate (left) and Ir DHC (right) on α-Fe_2O_3. a, a' Survey scans revealing that the only elements present are Fe, O, C, Ir, C, Sn and I. **b, b'** The peaks at 65 eV and 62 eV correspond to Ir $4f_{5/2}$ and Ir $4f_{7/2}$, respectively. Compared with Ir intermediate (**c, d**), high resolution spectra of C and N confirm the absence of the organic ligands in Ir DHC (**c', d'**).

XPS was performed by the K-Alpha+ XPS (Thermo Scientific) with an Al X-ray source (incident photon energy 1486.7 eV) at the Center for Nanoscale Systems (CNS) at Harvard University. Each spectrum was collected with at least 20 scans. The fitting of the XPS data was performed using the Casa XPS software. For each spectrum, the peak position was calibrated by referring to the carbon 1s peak to 284.6 eV.

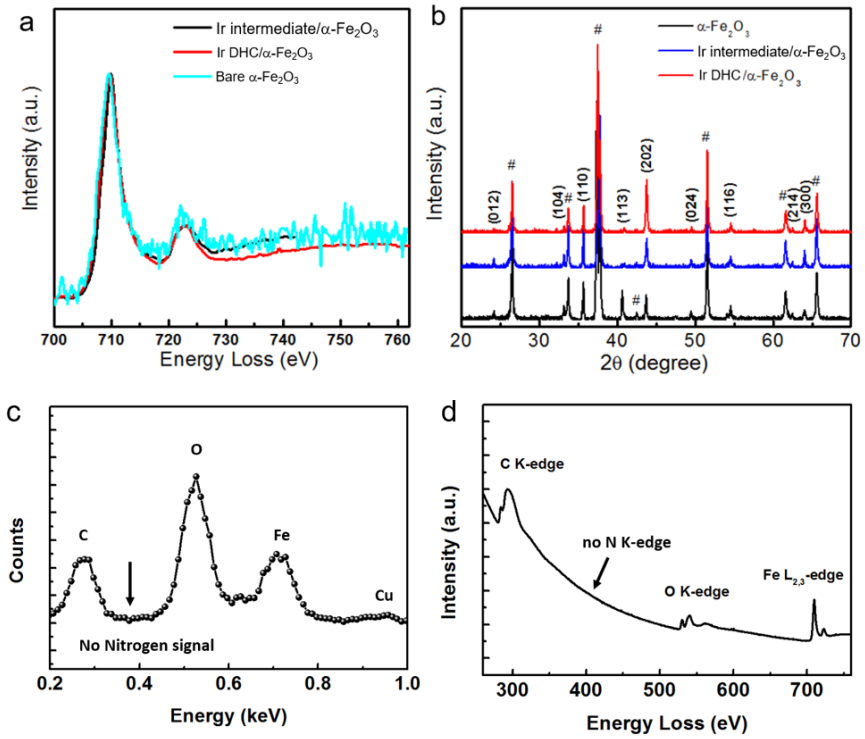

Fig. S3. a, EELS spectra of the Fe $L_{2,3}$-edge of Ir DHC on α-Fe_2O_3 and the reference samples. From the EELS data, it is clear that the valence state and the coordination environment of Fe do not change, demonstrating that the heterogenization process and the photochemical treatment do not fundamentally alter the α-Fe_2O_3 substrate. **b**, XRD patterns indicating that there are no Ir-containing crystalline NPs present after the heterogenization process and the photochemical treatment. The # symbol represents the peaks of SnO_2, which were due to the conductive substrate. **c**, EDS spectrum between 0.2 and 1.0 keV of Ir DHC. The EDS peak value of N K-edge should be 0.392 keV, which is absent in this spectrum. **d**, EELS spectrum from surface region of Ir DHC. The EELS peak of N K-edge should be at 401 eV, which is absent in the EELS spectrum. These data strongly support that the N-containing ligands have been successfully removed by the simple photochemical treatment.

XRD measurements were obtained on PANalytical X'Pert Pro diffractometer using Cu Kα radiation. For all samples, the scan rate varied from 6° /min (for wide range 20° to 90°) to 0.6° /min (for narrow range).

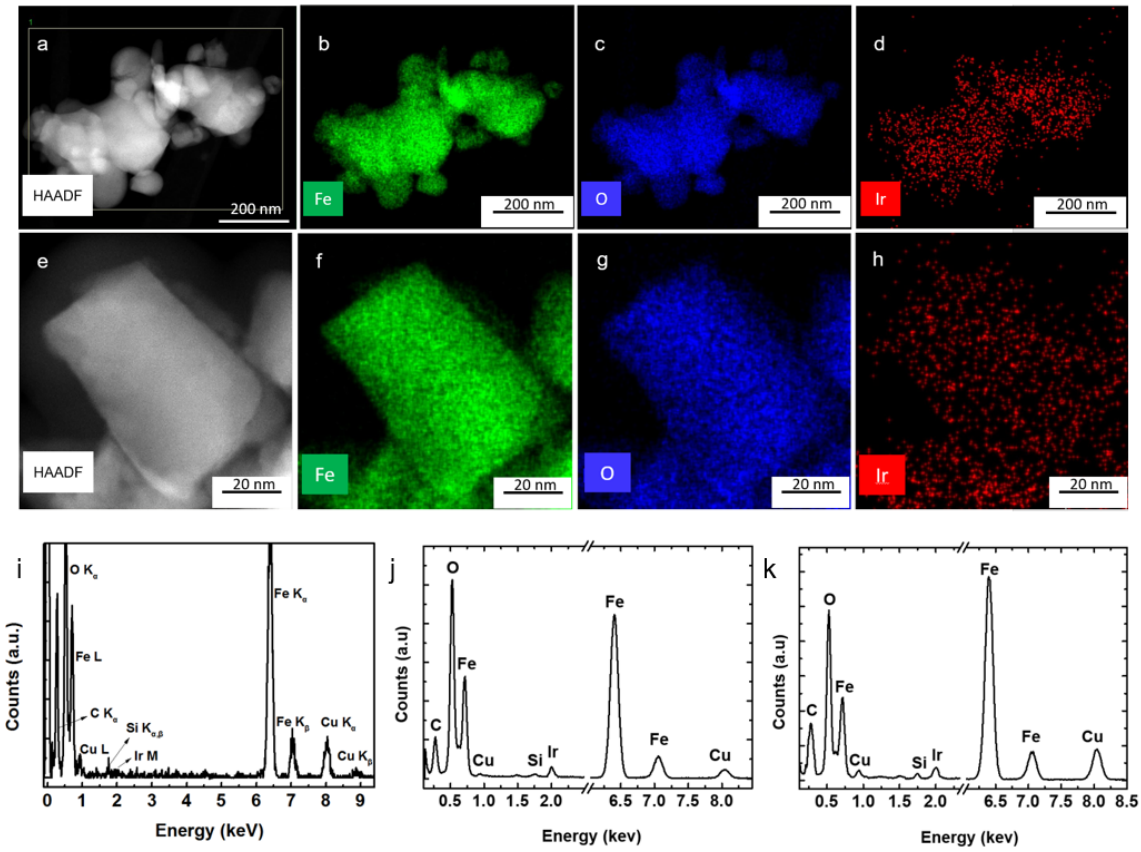

Fig. S4. STEM characterization of Ir DHC on α-Fe_2O_3. (**a** & **e**) HAADF-STEM images and (**b**-**h**) EDS elemental mapping of Fe, O and Ir in the same region at different magnifications. EDS spectra for Fig. 2d (**i**), Fig. S4a (**j**) and Fig. S4e (**k**). We highlight the uniformity of the Ir distribution.

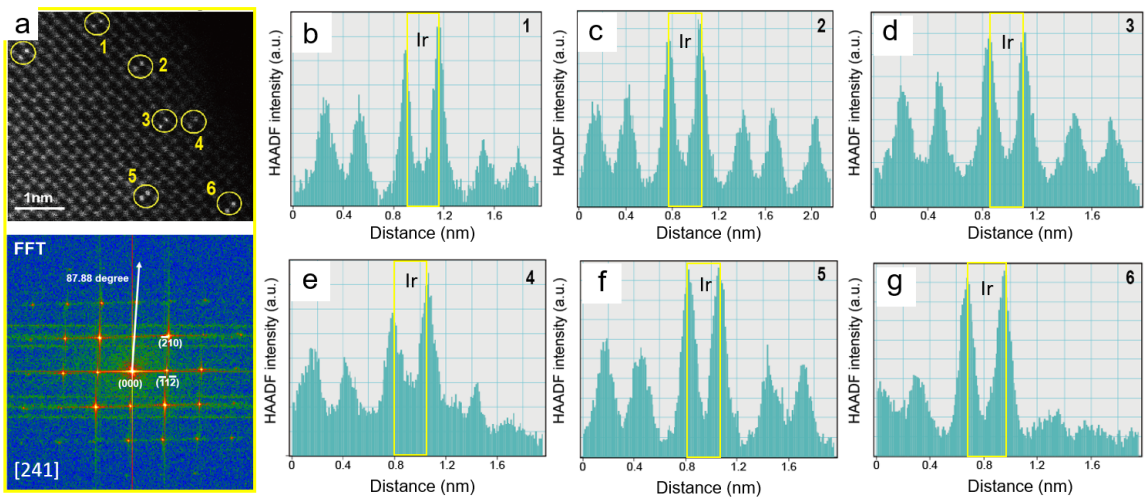

Fig. S5. STEM characterization of Ir DHC on α-Fe_2O_3 along the zone axis [241]. **a**, HAADF-STEM image and the corresponding fast Fourier transform diffraction pattern. (**b-g**) HAADF intensity line profiles taken along the atomic row marked by the circles. Based on the HAADF intensity profiles, the sharp two bumps are attributed to the existence of two Ir atoms whose atomic number (Z=77) is higher than Fe (Z=26).

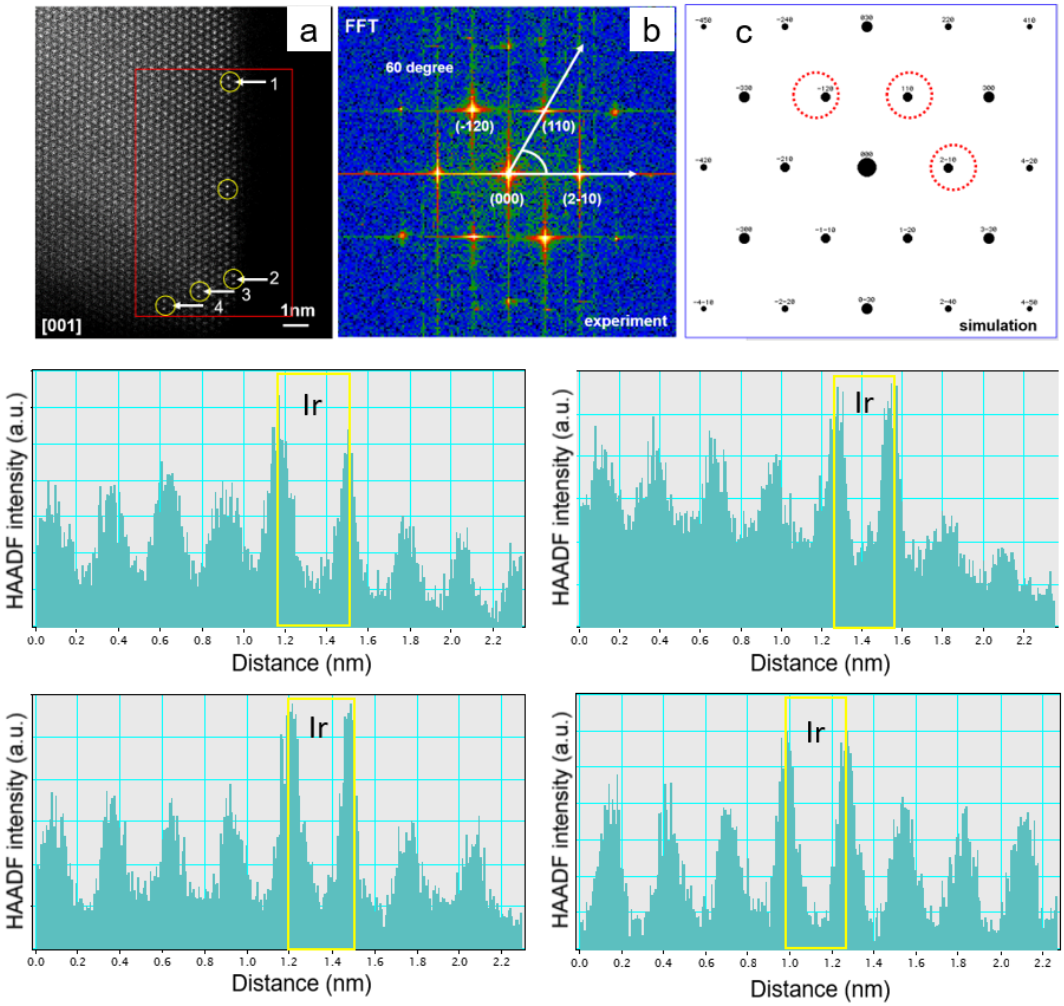

Fig. S6. STEM characterization of Ir DHC on α-Fe_2O_3 along the zone axis [001]. (**a**) HAADF-STEM image and corresponding experimental fast Fourier transform diffraction pattern (**b**) and simulated diffraction pattern of [001]-oriented α-Fe_2O_3 (**c**). HAADF intensity line profiles were extracted along the atomic rows marked by circles, respectively.

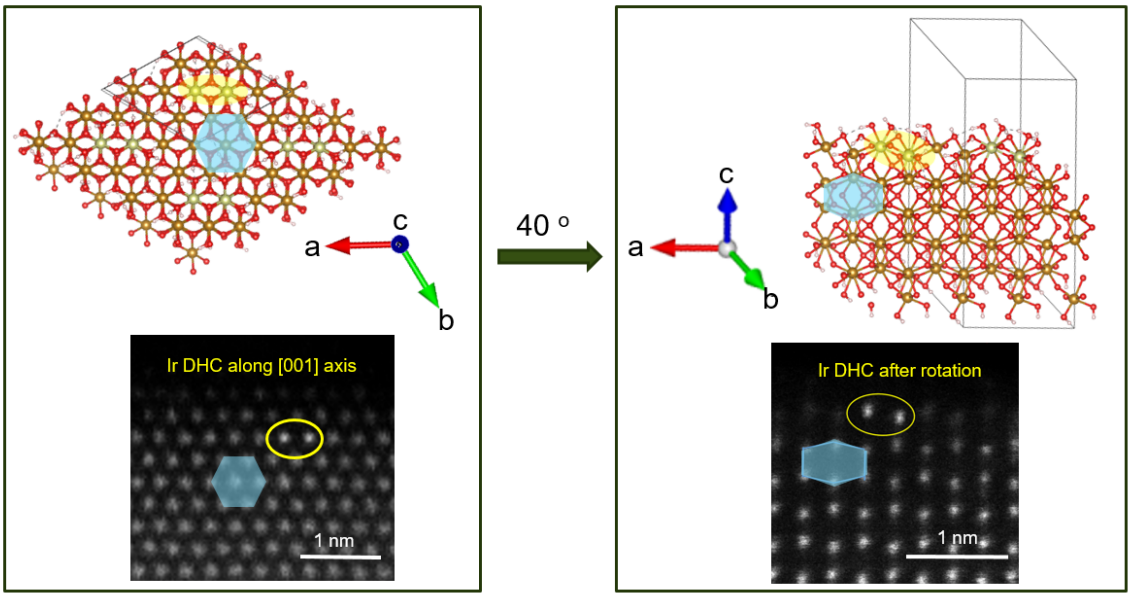

Fig. S7. Top view model and STEM image along [001] zone axis before (left) and after ca. 40° rotation (right). Scale bar: 1 nm

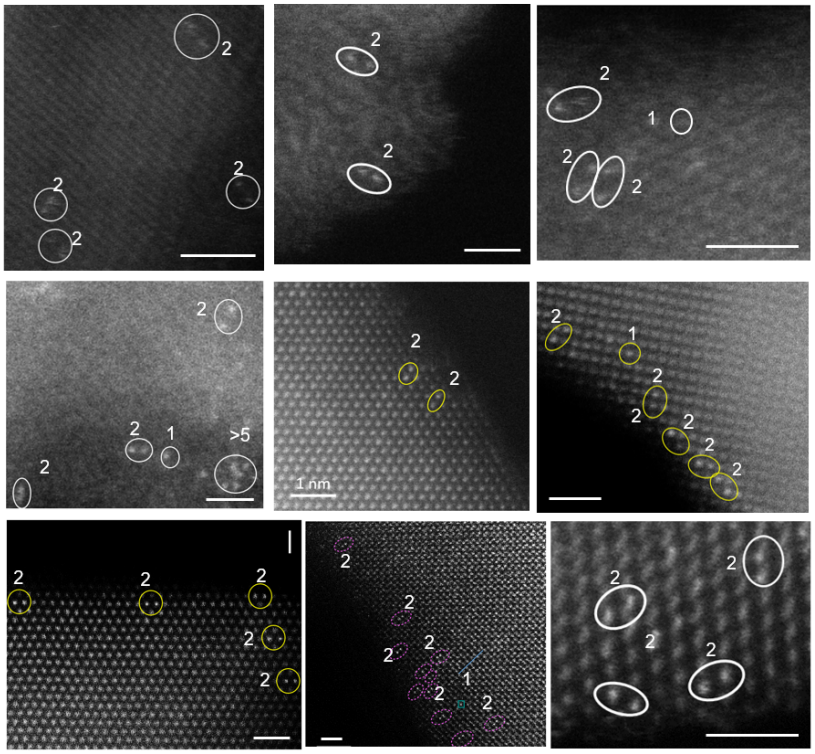

Fig. S8. More data of recorded Ir DHCs. Scale bars: 1 nm.

During the STEM test, approximately 110 Ir DHC units were observed. Of them, 38 Ir DHCs and 4 Ir SACs were successfully recorded at the atomic resolution. As is well known to the field, electron beam damage to the structure is the main technical challenge (Fig. S9).

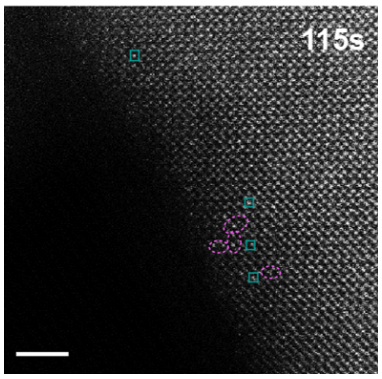

Figure S9. Evolution of Ir DHCs on α-Fe_2O_3 during electron beam exposure for 115 s in the same region with Fig. 4c-e in the main text. Scale bar: 2 nm.

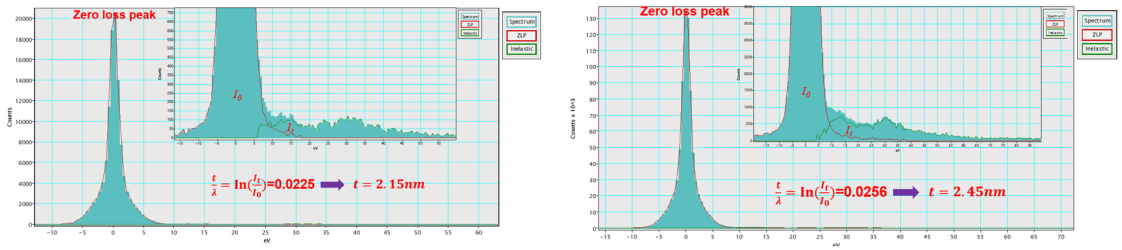

Fig. S10. $\ln(\frac{I_t}{I_0})$ analysis by the Digital Microscopy (DM) software program

The size of Fe_2O_3 nanoparticles in DHC sample is approximately 50-100 nm. For HAADF-STEM imaging, we focused on the edge regions of the nanoparticles, which are much thinner than the center regions. The thickness of the thin area where the Ir DHCs were observed was calculated by the Zero-loss peak (ZLP) using the EELS spectra. By measuring and analyzing the ZLP spectra, we obtained the thickness information by multiplying the value of $\ln(\frac{I_t}{I_0})$ and the calibrated effective plasmon mean free path of inelastic scattering (λ).

$$\frac{t}{\lambda} = \ln(\frac{I_t}{I_0})$$

Here t is the thickness, λ is an inelastic mean free path (IMFP) for the material, I_0 is the area under ZLP and I_t is the total area under the whole spectrum. An absolute thickness measurement requires knowledge of the IMFP, which depends on the specimen material, electron energy and collection semi-angle. λ obtained directly from the ZLP has an average error of 10%. It can be further calibrated by the convergent beam electron diffraction (CBED) technique. For this purpose, we first chose a thicker area (ca. 100 nm) of a typical sample for the thickness measurement by CBED (with an error of ca. 3%). Then, the ZLP spectra were acquired at the same area where the absolute thickness has already been determined by CBED. By comparing the thickness results by the two techniques, we calibrated the λ by ZLP under our experimental conditions, which was 95.52 (1/nm). The value of $\ln(\frac{I_t}{I_0})$ was obtained by analyzing the ZLP by using the Digital Microscopy (DM) software program (**Fig. S10**). Using EELS spectra from 10 representative areas (for a more accurate averaged value), we calculated the thickness of the samples where Ir DHCs were observed as 2.3 ± 0.15 nm.

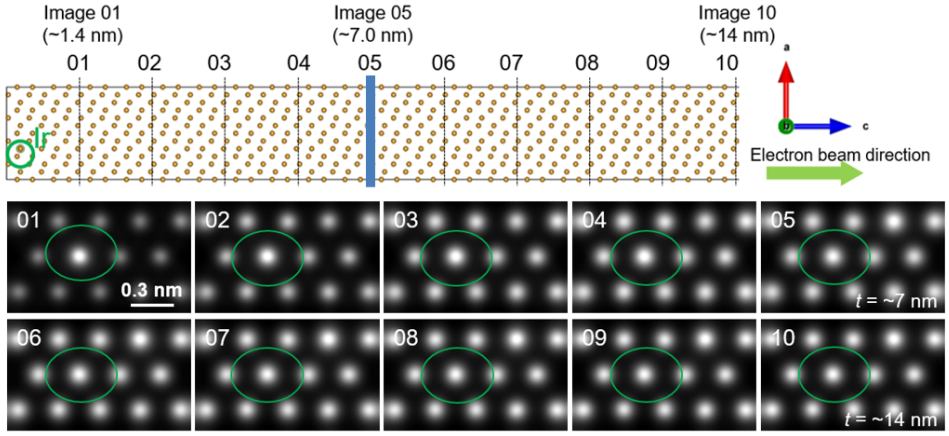

Fig. S11. Rigid model with one Ir atom on Fe_2O_3 with different thicknesses (top) and the corresponding simulated HAADF-STEM Z-contrast images (bottom)

HAADF-STEM simulations (**Fig. S11**) suggest that Ir atoms (atop the Fe atomic column) on the (001) surface would be indistinguishable if the thickness of Fe_2O_3 is > 7 nm.

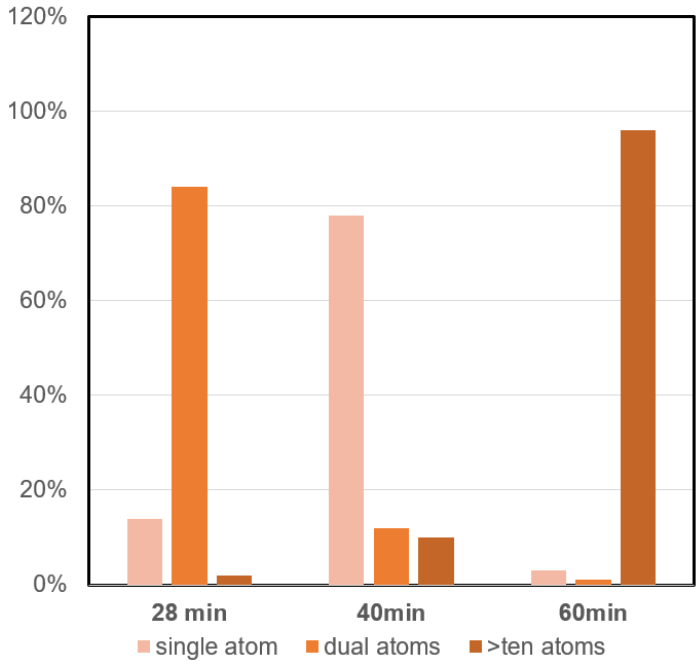

Fig. S12. Species distribution in samples by photochemical treatment for different durations.

When the Ir intermediate sample was treated by photochemistry for 28 min, dinuclear units account for over 80% of the observed species. By increasing the photochemical treatment duration, the O bridge in Ir-O-Ir is broken to form Ir-O single site. Further increase of the treatment duration promotes the aggregation of the Ir SACs to form NPs due to better mobility of Ir SACs on Fe_2O_3 than Ir DHCs.

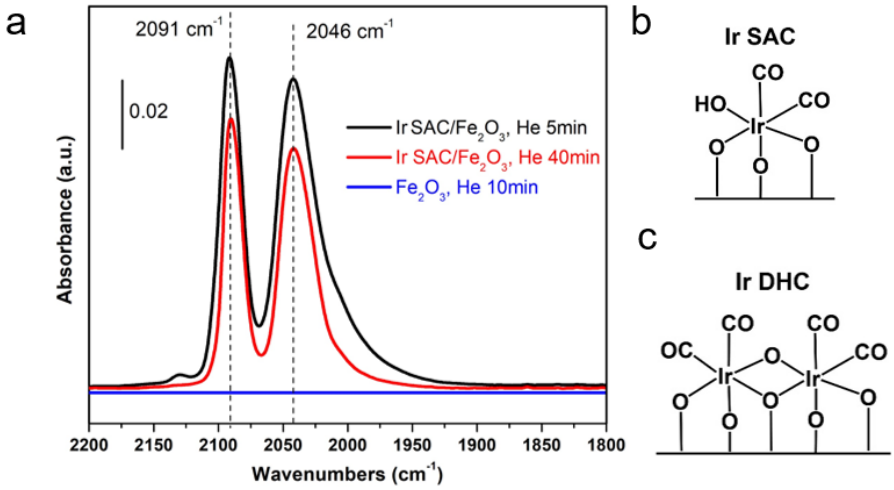

Fig. S13. *In situ* DRIFT spectra of Ir SAC/α-Fe_2O_3 and bare α-Fe_2O_3 in He flow after CO treatment at room temperature (**a**) and the proposed structures of CO bonding modes for Ir SAC (**b**) and Ir DHC (**c**).

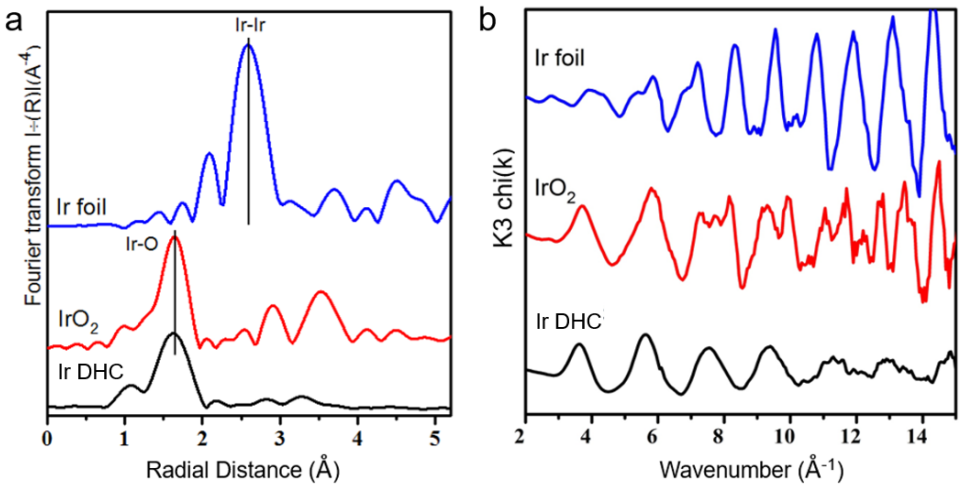

Fig. S14. Fourier transforms of Ir L3-edge EXAFS experimental data for Ir foil, IrO_2 and Ir DHC on SiO_2 (**a**) and the corresponding k^3-weighted EXAFS data (**b**).

To avoid interference from the post-edge of the Fe signal from the α-Fe_2O_3 substrate, as well as the potential Ir-Fe scattering pathways, EXAFS data were collected on a mesoporous silica SBA-15 substrate instead of on α-Fe_2O_3. The XANES spectra showed almost identical spectral features for Ir DHC on SBA-15 and on α-Fe_2O_3 substrate, proving that it is an appropriate substitute to collect the EXAFS signals from the substrate transferred from α-Fe_2O_3 to SBA-15. We do caution, however, that further research is needed to fully understand whether Ir DHCs form the same way they do on α-Fe_2O_3. The Fourier transformed EXAFS spectra indicate that there is one notable peak in the region 1 to 2 Å from the Ir-O contribution, with no peak in the region 2 to 3 Å from the Ir-Ir contribution. These would be characteristic peaks from Ir NPs. Compared with the spectrum of IrO_2, negligible signals have been observed in the position of 2.92 and 3.54 Å from the second shell scattering contribution of Ir DHC, indicating that the loss or weakening of the scattering from the second shell. This is consistent with the structure of the Ir DHC, where only one Ir-O-Ir exists, much fewer than the 10 scattering pathways for Ir-O-Ir of IrO_2.

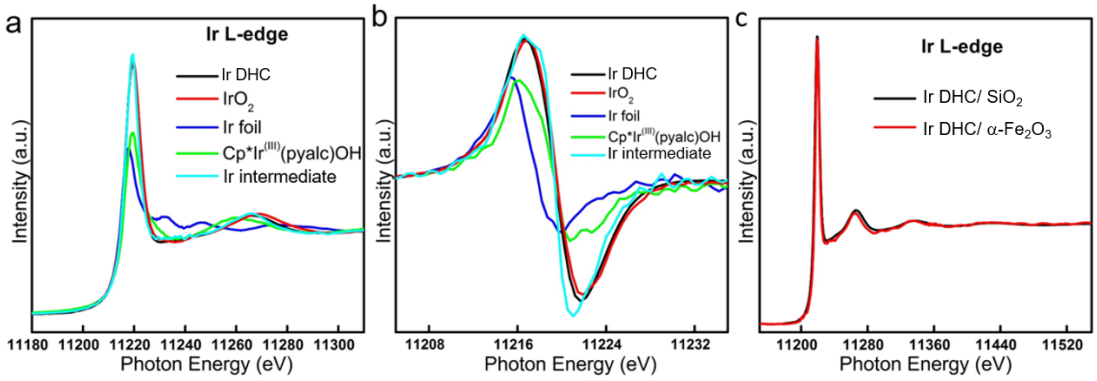

Fig. S15. Ir L3-edge XANES of Ir DHC, reference samples Ir foil, IrO_2, Cp*$Ir^{(III)}$(pyalc)OH and Ir intermediate (**a**). Corresponding first order derivative of the data (**b**). The comparison of Ir DHC on different substrates (**c**).

The XANES probes the transition from the core level to the conduction band, i.e., $2p_{3/2}$ to $5d_{5/2}$ for Ir L_3-edge (5). The diversities of the intensity and the position of the white line (WL) peak provide a basis to examine the electronic structure of the samples. The stronger WL peak intensity and higher photon energy peak represent a higher valence state. The XANES spectra suggest that the valence state of Ir DHC is IV. Importantly, there is no observable difference between the Ir DHC XANES signals on SiO_2 and α-Fe_2O_3.

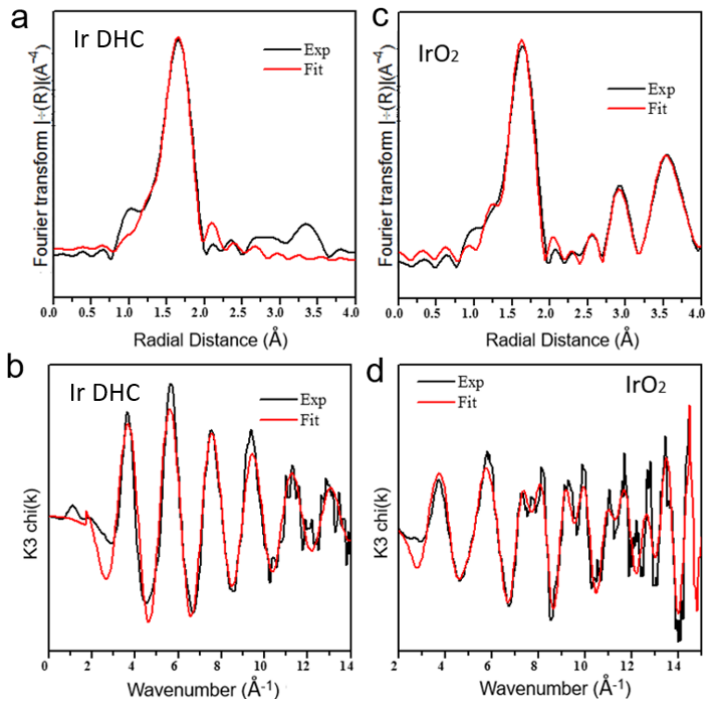

Fig. S16. Fourier transforms of Ir L3-edge EXAFS experimental data for Ir DHC and fitting for Ir DHC in R space (**a**) and k space (**b**). Fourier transforms of Ir L3-edge EXAFS experimental data for IrO_2 and fitting data for IrO_2 in R space (**c**) and k space (**d**).

Table S1. Structural parameters obtained from the fits of the EXAFS spectra.

Scattering Path	CN	R(Å)	σ^2(Å^2)	ΔE_0(eV)
Ir-O (Ir DHC)	5.85	2.01625	0.00458977	11.23889765
Ir-O (IrO_2)	6	1.98960	0.00959470	14.09129971

CN, coordination number; R, bonding distance; σ^2, Debye-Waller factor; ΔE_0 shift in absorption edge energy.

Fitting parameters: Δk=3-14 Å^{-1}, dk=0 Å^{-1}, ΔR=1-2.2 Å^{-1}, S_0^2=0.90

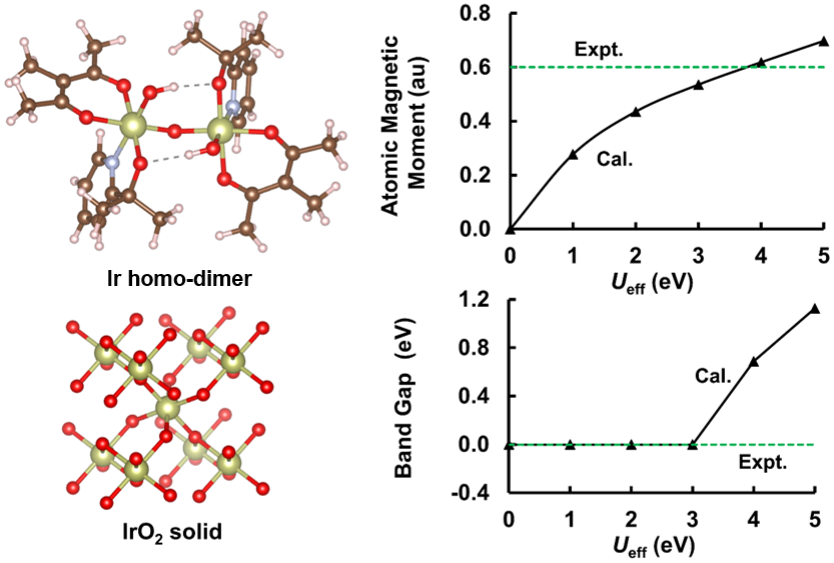

Fig. S17. Determination of the correct U_{eff} parameters for Ir by fitting to the experimental atomic magnetic moment of Ir homo-dimer (top right) and band gap of IrO_2 (bottom right).

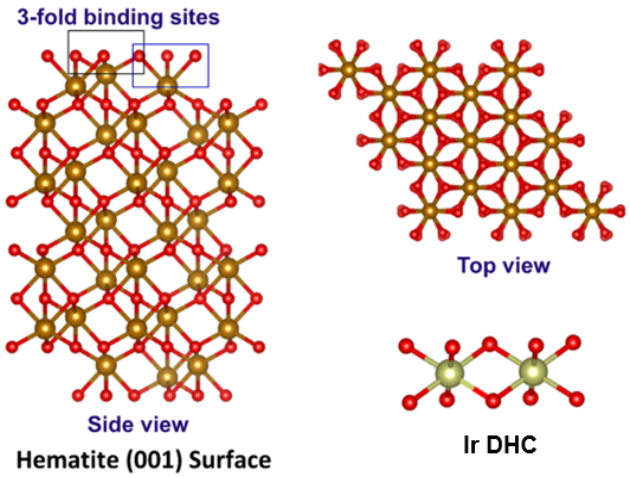

Fig. S18. Two nearby three-fold O binding sites on the α-Fe_2O_3 (001) surface and a proposed Ir DHC structure.

Table S2. Comparison of calculated and experimental properties of bulk α-Fe_2O_3 (U_{eff} = 4 eV)

Properties	PBE	PBE+*U*	Experimental
a / Å	5.00	5.06	5.03
c / Å	13.78	13.83	13.75
γ / degree	120.0	120.0	120.0
dFe−O1 / Å	1.92	1.96	1.94
dFe−O2 / Å	2.13	2.12	2.11
Atomic magnetic moment (μB)	3.52	4.15	4.90
Eg (eV)	0.7	2.3	2.0-2.2

Table S3. Comparison of representative Ir-based catalysts for solar water oxidation.

Materials	*Preparation Method*	V_{on} *(V vs. RHE)*	*Photocurrent density @ 1.23 V vs. RHE (mA/cm²)*	*Per Ir atom turnover frequency (h^{-1})*	*Ref.*
α-Fe₂O₃/IrO₂	Electrodeposition	1.1	0.15	N/A	(29)
α-Fe₂O₃/IrO₂	Photoelectro-deposition	0.6	0.8	1.7	(22)
α-Fe₂O₃/IrO₂	Electrophoresis	0.8	3.2	N/A	(28)
α-Fe₂O₃/anchored Ir complex (1)	Heterogenization	0.6	1.1	83	(25)
α-Fe₂O₃/anchored Ir complex (2)	Heterogenization	1.2	N/A	N/A	(27)
α-Fe₂O₃/Ir DHC	Photochemical deposition	0.55	1.51	212	This work
α-Fe₂O₃/Ir SAC	Photochemical deposition	0.63	1.01	80	This work
α-Fe₂O₃/Ir NPs	Post-annealing	0.63	0.89	42	This work

The turnover frequency (TOF) was estimated using the following equation. Here, we assume a four-electron process for water oxidation at 1.23 V vs. RHE:

$$\mathrm{TOF} = \frac{I_{sample} - I_{bare}}{4FN_{Ir}}$$

where I_{sample} is the current passed through the Fe_2O_3 electrode with catalyst ($C/s{\cdot}cm^2$), I_{bare} is the current passed through the Fe_2O_3 bare electrode ($C/s{\cdot}cm^2$), F is the Faraday constant (96485 C/mol), and N_{Ir} is the amount of iridium loading on the electrode surface (mol/cm^2).

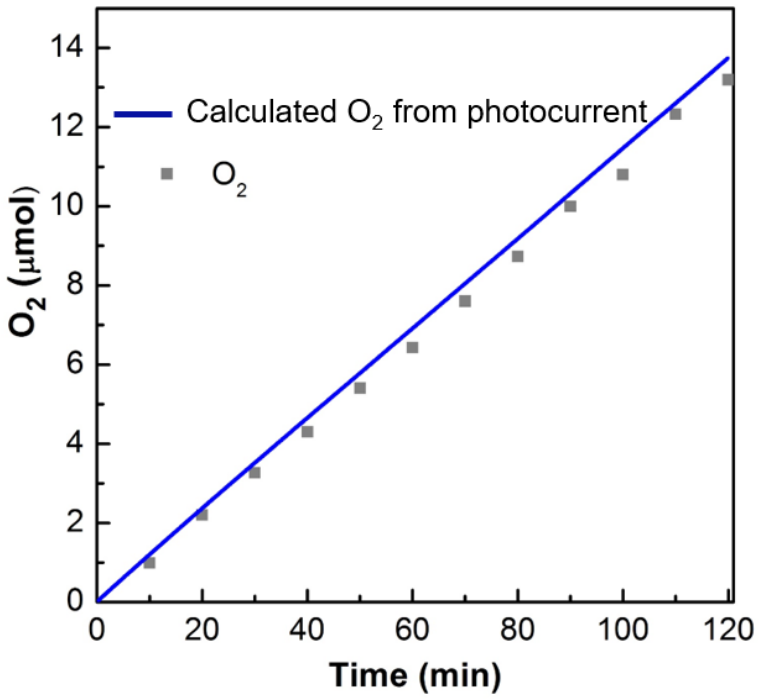

Fig. S19. Detection of evolved O_2 by Ir DHC on α-Fe_2O_3. Electrolyte: 0.1M KNO_3 (pH adjusted to 6.0 by KOH (pH 8.0)); lighting condition: AM 1.5 illumination at 100 mW cm^{-2}; applied potential: 1.23 V vs. RHE.

The evolved O_2 was detected *in situ* using a Clark-type BOD oxygen electrode (Thermo Scientific 9708 DOP). The surface area of the electrode was increased to ca. 0.5 cm^2 for increased O_2 production to minimize the relative experimental errors. The working electrode, the reference electrode, the counter electrode and the oxygen sensor were sealed in a three-neck flask with 130 mL 0.1M KNO_3 by rubber stoppers wrapped with parafilm and high vacuum grease to prevent leaks. N_2 gas was used to purge out dissolved O_2 and gaseous O_2 in the headspace for at least 1 h. Afterwards, the N_2 purging needle was removed. The oxygen sensor was typically allowed to stabilize to 0 ppm for at least 20 min. The O_2 yield during electrolysis was read directly using a pH meter connected to the oxygen sensor.

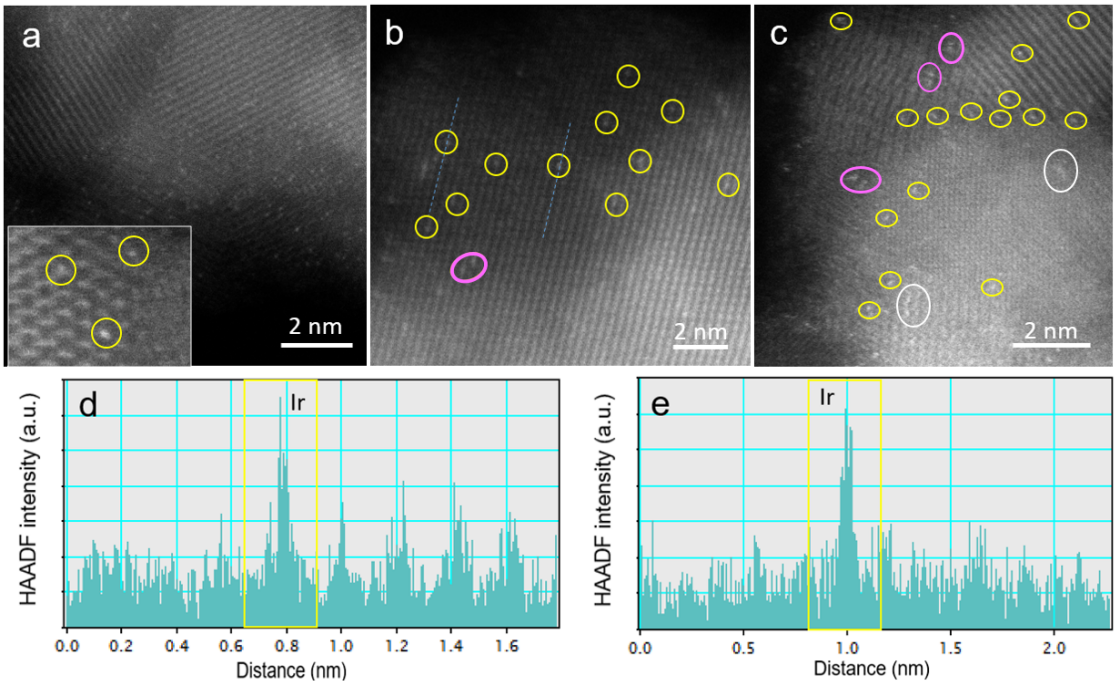

Fig. S20. STEM characterization of Ir SAC on α-Fe_2O_3. Bright points represent a single Ir atom. Yellow circle represents the dominated species single atom. Peachblow and white circle represents the very limited amount of dinuclear species and nanoparticles. HAADF intensity line profiles were taken along the atoms. Based on the HAADF intensity profile, the sharp bumps are attributed to the existence of a single Ir atom with a diameter of ca. 0.1 nm.

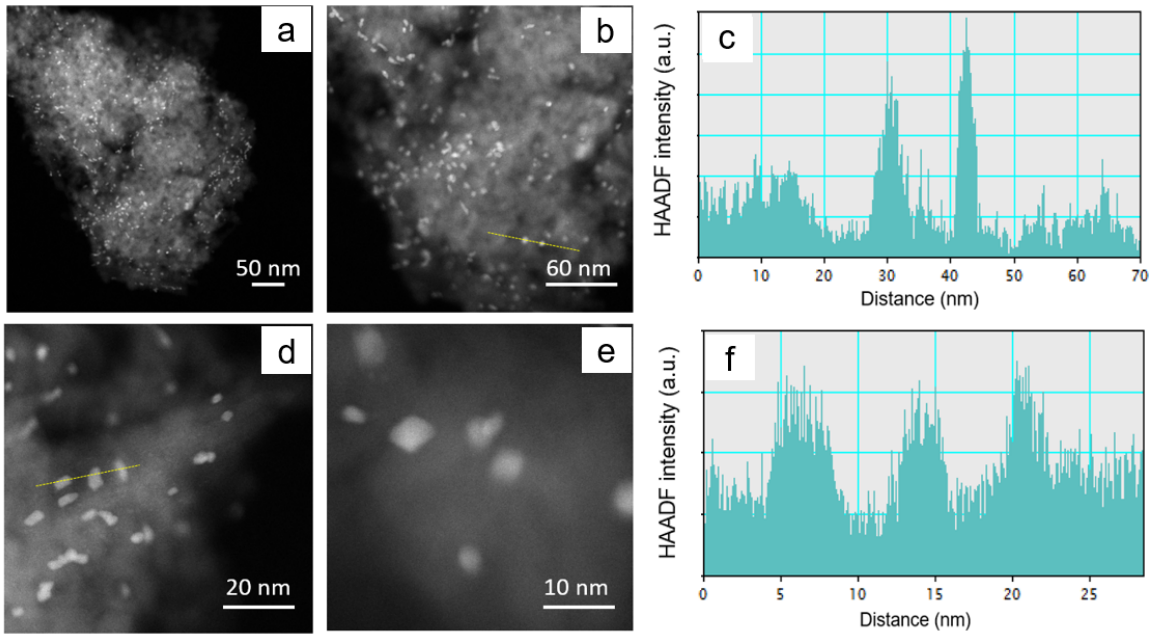

Fig. S21. STEM characterization of Ir-based NPs on α-Fe_2O_3. Bright points represent aggregated Ir-based NPs. HAADF intensity line profiles were taken along the nanoparticles. Based on the HAADF intensity profile, the sharp bumps are attributed to the existence of Ir-based NPs with diameters of ca. 2 nm.

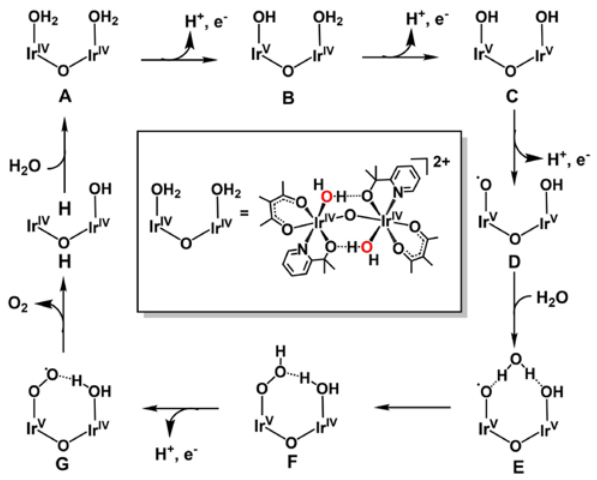

Fig. S22. Proposed schematic catalytic cycle of Ir homo-dimer.

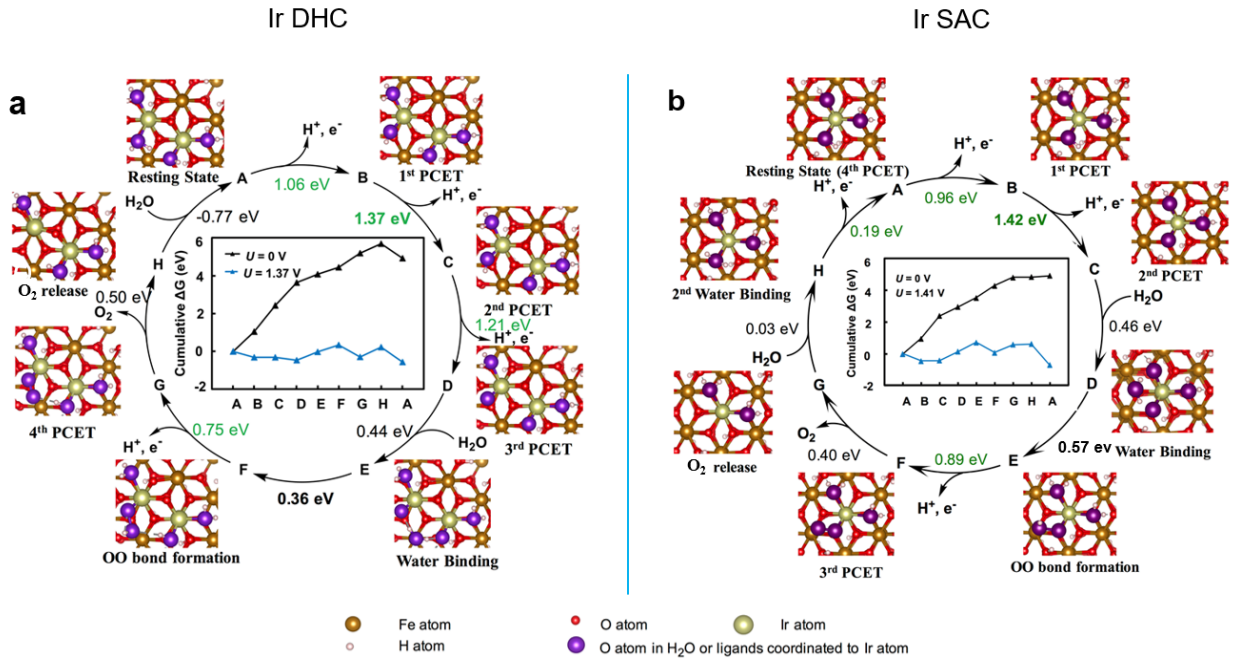

Fig. S23. DFT optimized structures of intermediates and calculated reactions free energies at zero bias potential (U = 0 V) of Ir DHC (**a**) and Ir SAC (**b**). Reaction free energies in green correspond to proton-coupled electron transfer steps which could be driven by applying bias potentials. Inset: calculated cumulative ΔG at bias potential U = 0 and 1.37 V (for Ir DHC) and 1.42 V (for Ir SAC).

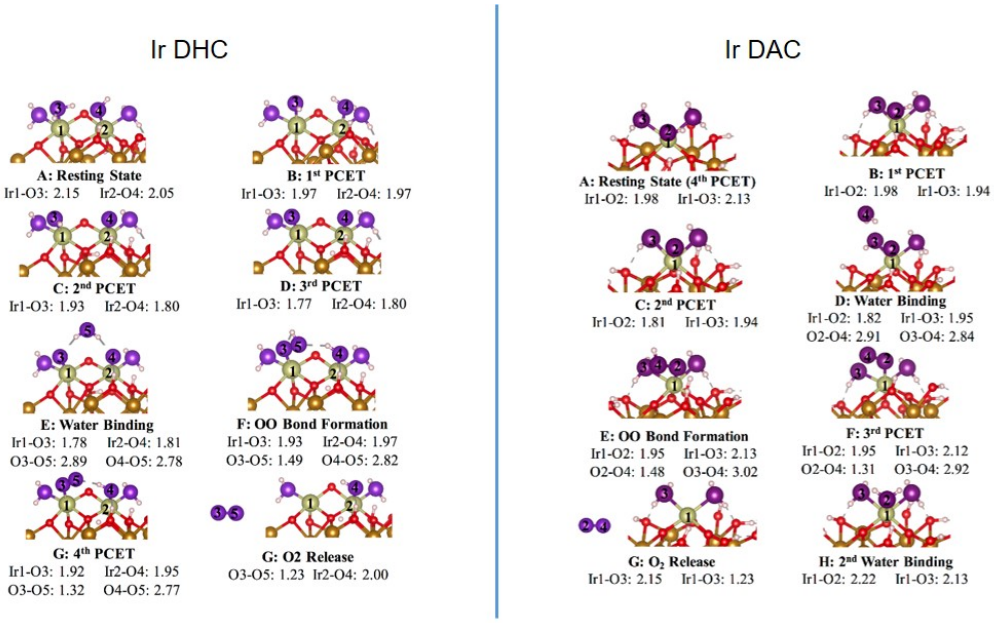

Fig. S24. Side view and lengths of key bonds of DFT optimized structures of intermediates of Ir DHC (left) and Ir SAC (right).

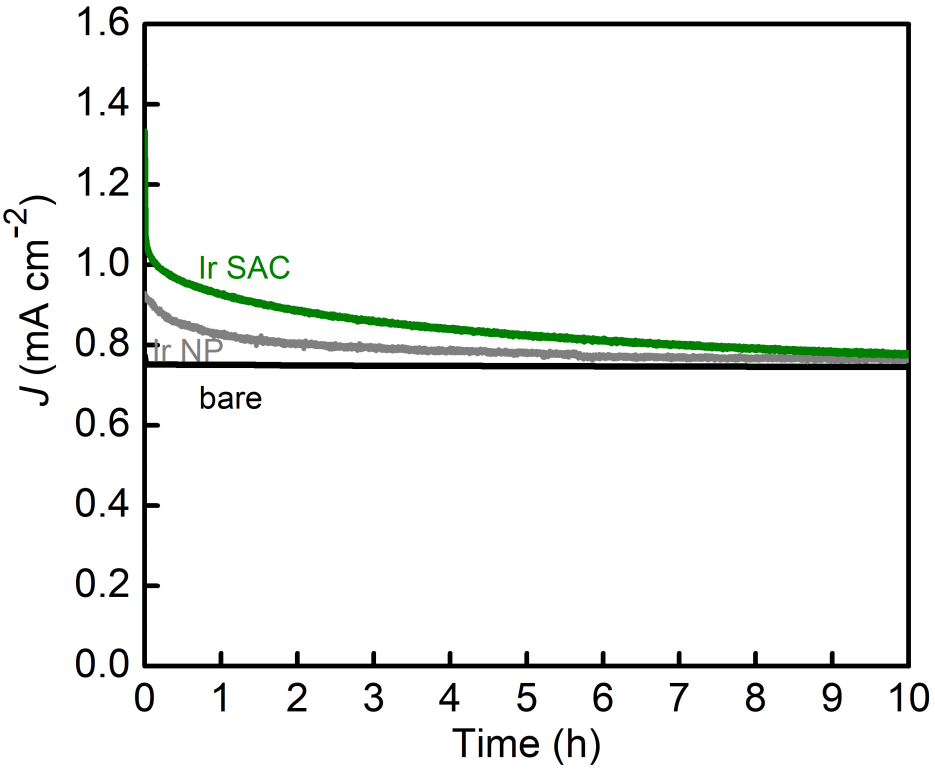

Fig. S25. Chronoamperometry showing the stability of reference samples over 10 h at 1.23 V vs. RHE in 0.1M KNO_3 (pH 6.0).

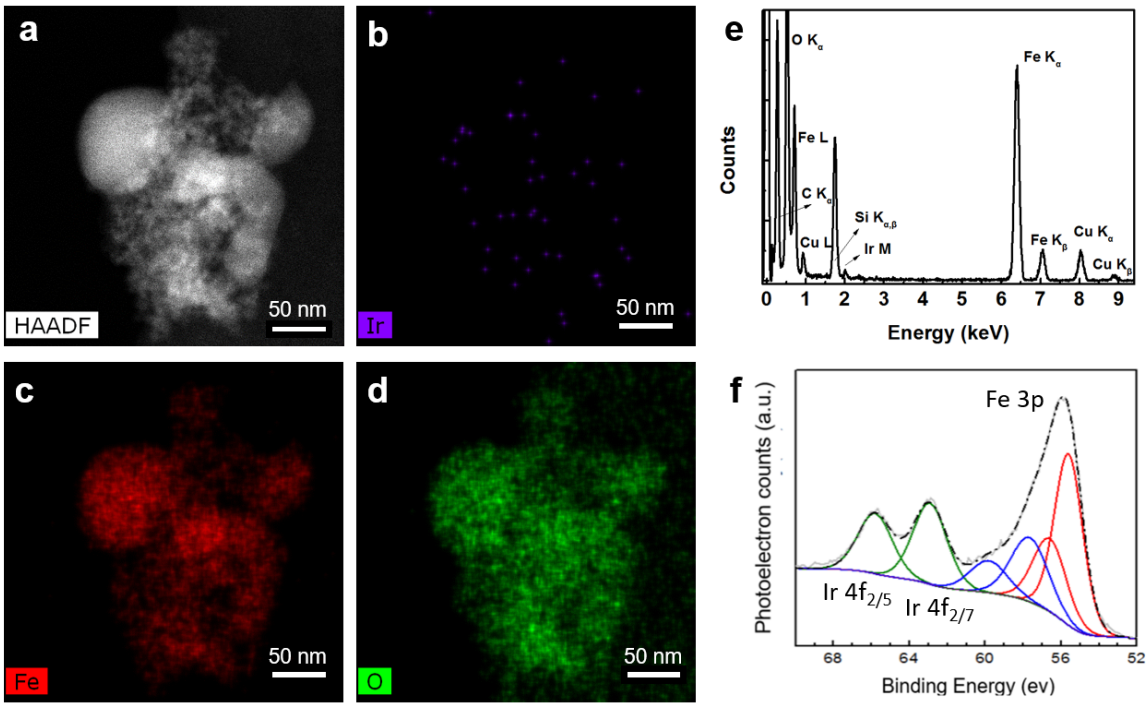

Fig. S26. Characterization of Ir DHC after 10h chronoamperometry stability test. (**b-d**) Elemental mapping of Ir, Fe and O, respectively. The corresponding HAADF-STEM image for the mapped area is shown in **a**. Aggregation of Ir atoms was not observed. (**e**) The peak at 2 keV is ascribed to the Ir M-edge. (**f**) The XPS peaks at 65 eV and 62 eV correspond to Ir $4f_{5/2}$ and Ir $4f_{7/2}$, respectively. The features are similar to fresh Ir DHC on α-Fe_2O_3.

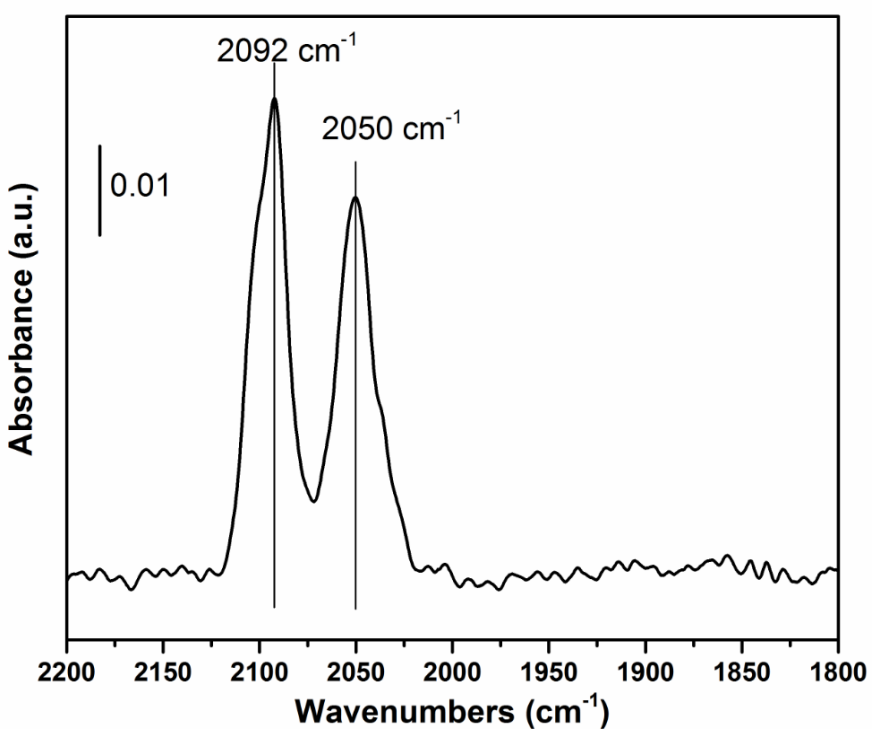

Fig. S27. *In situ* DRIFT spectra of Ir DHC on α-Fe_2O_3 after 10 h stability test in He after CO treatment at room temperature. The features are similar to fresh Ir DHC on α-Fe_2O_3.

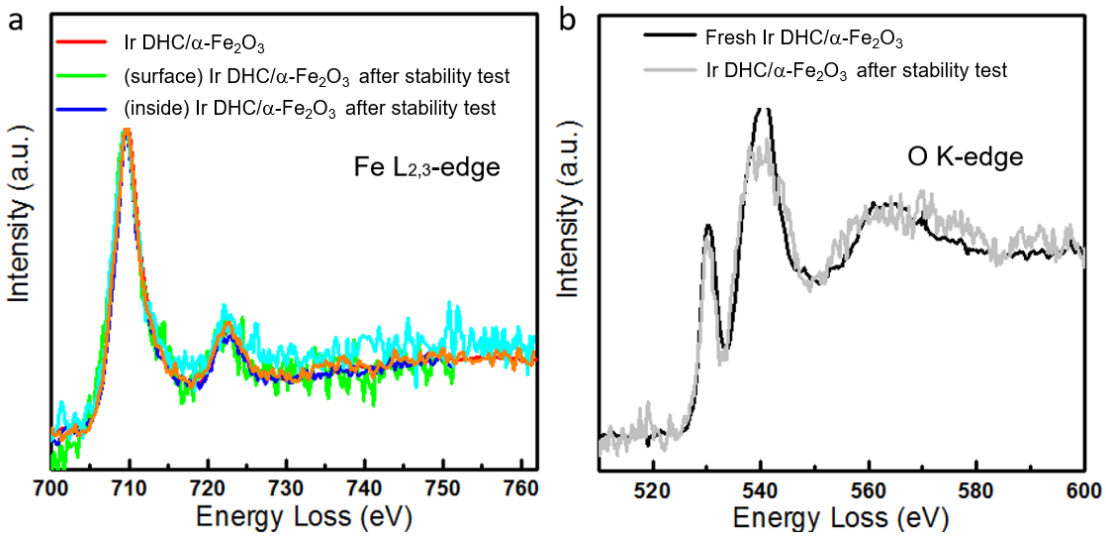

Fig. S28. EELS spectra of Fe $L_{2,3}$ edge (**a**) and O K edge (**b**) of Ir DHC on α-Fe_2O_3 before and after 10 h electrolysis.

References for SI

1. Thomsen JM, *et al.* (2014) Electrochemical activation of Cp* Iridium complexes for electrode-driven water-oxidation catalysis. *J. Am. Chem. Soc.* 136(39):13826-13834.
2. Jang JW, *et al.* (2015) Enabling unassisted solar water splitting by iron oxide and silicon. *Nat. Commun.* 6:7447.
3. Barthel. J (2017) Dr. Probe-STEM Simulation Software. *http://www.erc.org/barthel/drprobe/;accessed 8.2.2018*.
4. Momma K & Izumi F (2011) VESTA 3 for three-dimensional visualization of crystal, volumetric and morphology data. *J. Appl. Crystallogr.* 44:1272-1276.
5. Ravel B & Newville M (2005) ATHENA, ARTEMIS, HEPHAESTUS: data analysis for X-ray absorption spectroscopy using IFEFFIT. *J. Synchrotron. Radiat.* 12:537-541.
6. Dudarev SL, Botton GA, Savrasov SY, Humphreys CJ, & Sutton AP (1998) Electron-energy-loss spectra and the structural stability of nickel oxide: An LSDA+*U* study. *Phys. Rev. B* 57(3):1505-1509.
7. Nørskov JK, *et al.* (2004) Origin of the overpotential for oxygen reduction at a fuel-Cell cathode. *J. Phys. Chem. B* 108(46):17886-17892.
8. Liao P, Keith JA, & Carter EA (2012) Water oxidation on pure and doped hematite (0001) surfaces: prediction of Co and Ni as effective dopants for electrocatalysis. *J. Am. Chem. Soc.* 134(32):13296-13309.
9. Rossmeisl J, Logadottir A, & Nørskov JK (2005) Electrolysis of water on (oxidized) metal surfaces. *Chem. Phys.* 319(1–3):178-184.